JOURNAL OF MATERIALS SCIENCE 27 (1992) 3266–3280

Characterization of inertia–friction welds between a rapidly-solidified Al–Fe–Mo–V alloy and IM 2024–T351

H. H. KOO, K. SAMPATH, W. A. BAESLACK III
Department of Welding Engineering, The Ohio State University, Columbus, OH 43210, USA

The structures, mechanical properties and fracture behaviour of inertia–friction welds produced between rapidly-solidified/powder metallurgy (RS/PM) Al–9Fe–3Mo–1V (wt %) and ingot metallurgy (IM) 2024–T351 aluminium were investigated. Visual examination showed the axial displacement experienced by the specimens during welding and the degree of metal expulsion from the weld interface (i.e. "flash") to increase with an increase in axial force. The weld flash was observed to originate principally from the IM 2024–T351, which was consistent with the lower elevated-temperature strength of this precipitation-hardened alloy. Although the weld interface region remained nearly flat in welds produced using low axial force, this surface became increasingly curved (concave into the Al–9Fe–3Mo–1V alloy) with an increase in axial force. Microstructure analysis using both light and analytical electron microscopy characterized the heat- and deformation-affected zones (HDZs) in each of the base metals and the weld interface regions. The HDZ directly adjacent to the weld interface in the IM 2024–T351 exhibited fine, recrystallized alpha aluminium grains and an absence of S′ precipitates present in the base metal microstructure. The HDZ directly adjacent to the weld interface in the Al–9Fe–3Mo–1V exhibited fine alpha grains and fine, spherical and acicular dispersoids, which in part originated from the plastic deformation and fracture of coarse base metal dispersoid particles. The extent of this dispersoid-refined region was greatest at the centre of the weld as opposed to the outer periphery, and in the low rather than the high axial force weld. At the weld interface in the vicinity of the axial centre line, the occurrence of highly localized mechanical mixing between the two alloys was determined using both light and electron microscopy and electron-microprobe analysis techniques.

Microhardness traverses showed relatively little variation in hardness across the weld interface and an absence of hardness degradation at any location relative to the unaffected base metals. Room-temperature transverse-weld tensile testing showed tensile strengths to range between 85 and 90% of the RS/PM base metal, with fracture occurring in the Al–9Fe–3Mo–1V HDZ remote from the weld interface. Three-point guided bend testing also revealed fracture to occur in the Al–9Fe–3Mo–1V HDZ. SEM fractographic analysis of the fracture surfaces found fracture in the Al–9Fe–3Mo–1V to involve microvoid formation at dispersoid/alpha aluminium interfaces and subsequent ductile rupture in the alpha aluminium matrix.

1. Introduction

Al–9Fe–3Mo–1V (wt %) belongs to a relatively new family of dispersion-strengthened aluminium alloys produced by rapid solidification and powder metallurgy (RS/PM) processing [1]. These alloys are based on hypereutectic Al–Fe base compositions with ternary and quaternary additions of Mo, Ce, V and/or Si. RS/PM processing of these novel chemistries generates a microstructure comprising a uniform distribution of sub-micrometer-sized dispersoid particles in a fine-grained (1 to 2 μm) alpha aluminium matrix. The ternary and quaternary alloy additions are characterized by low solid solubility and solid-state diffusivity in alpha aluminium. In addition to forming complex, metastable dispersoids, these alloy additions also reduce the interfacial energy or lattice disregistry across the dispersoid particle/alpha aluminium matrix interface, and thereby provide a minimal driving force for particle coarsening at elevated temperatures. The microstructural features exhibited by these alloys provide high room-temperature strength and excellent elevated-temperature mechanical properties. As shown in Fig. 1, the Al–9Fe–3Mo–1V alloy exhibits elevated-temperature strength superior to that of IM 2024–T351, and from a specific strength standpoint compares favourably with Ti–6Al–4V between 150 and 300 °C [2–4].

In recent years, several weldability investigations

0022–2461

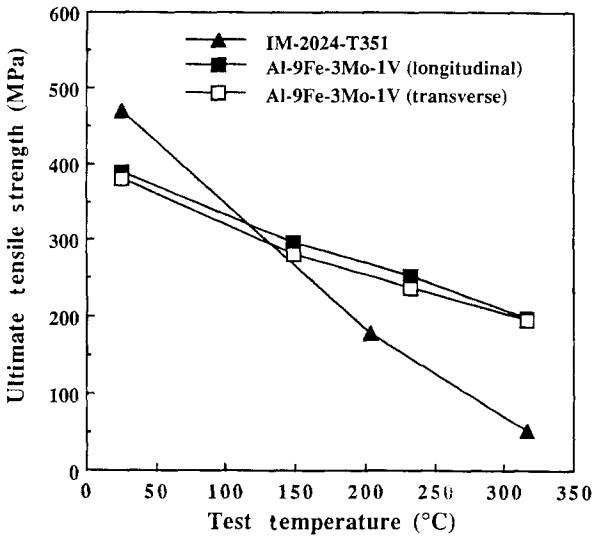

Figure 1 Tensile strength against test temperature for RS/PM Al–9Fe–3Mo–1V and IM 2024–T351 [3, 4].

have developed effective joining approaches for RS/PM dispersion-strengthened aluminium alloys. One approach is based on the utilization of high-energy density fusion welding methods such as pulsed Nd:YAG laser welding [5] and electron beam welding [6] to join alloys which contain a low residual hydrogen content (< 1 ml per 100 g Al). The rapid cooling rates which characterize these processes have been shown to recreate a rapidly solidified fusion zone and minimize structural coarsening in the adjacent heat-affected zone. Alternative joining approaches including capacitor-discharge welding [7] and solid-state welding methods such as inertia–friction welding [8] have also been demonstrated effectively to join RS/PM base materials which contain a high residual hydrogen content (> 5 ml per 100 g Al). In contrast to fusion welding, solid-state welding methods avoid melting and resolidification, and thereby preclude the formation of weld defects such as porosity and solidification cracking. Further, these methods also enable optimization of specific process parameters to restrict the heat- and deformation-affected zone (HDZ) to a relatively narrow region.

A previous investigation evaluated structure/property/fracture relationships in inertia–friction welds produced between cylindrical sections of an RS/PM Al–Fe–Ce alloy with similar (Al–Fe–Ce) and dissimilar (IM 2024) alloy combinations [8]. That investigation determined that the utilization of a sufficiently high weld-axial force produced joints with room-temperature weld mechanical properties comparable to those of the base material. However, the limited spatial resolution of light and scanning electron microscopy (SEM) utilized in that study precluded detailed microstructural characterization of the weld region. A subsequent investigation used transmission electron microscopy (TEM) to characterize the weld interface region of similar-alloy inertia–friction welds in an RS/PM Al–9Fe–3Mo–1V (wt %) alloy [9]. This analysis showed that during welding extensive plastic deformation occurs at the weld interface which fractures the coarse base metal dispersoid particles into fine-sized acicular and spherical particles, thereby improving the dispersoid density and correspondingly the weld-zone hardness and strength. The present investigation was performed to complement this earlier study on Al–9Fe–3Mo–1V by characterizing in detail the microstructure across dissimilar alloy inertia–friction welds produced between this RS/PM alloy and the conventional, ingot metallurgy alloy 2024–T351.

2. Experimental Procedure

2.1. Materials

The RS/PM Al–8.7Fe–2.8Mo–1V (actual chemistry, wt %) alloy originated as rapidly-solidified powder produced by Pratt and Whitney Aircraft's "rapid solidification rate" (RSR) process. In this process, a rapidly spinning disc produces centrifugal forces and disperses a thin stream of melt into fine-sized, spherically symmetric liquid droplets. The concurrent application of a helium gas shroud produces forced convective cooling conditions ranging from 10^4 to $10^6\,^{\circ}C\,s^{-1}$ and promotes rapid solidification of the individual liquid droplets. The helium gas also minimizes surface oxide and hydrate formation. Following atomization, the powder particles were hot-vacuum degassed and extruded into a 250-mm-diameter cylinder.

In the present investigation, the RS/PM Al–9Fe–3Mo–1V alloy was welded in the as-extruded condition, while the IM 2024 was welded in the extruded and heat-treated condition (T351 temper). Inertia–friction welding was performed using cylindrical specimens (22.2 mm in diameter, 76.2 mm in length). The longitudinal specimen directions for the RS/PM Al–9Fe–3Mo–1V and IM 2024–T351 alloys were oriented transverse and parallel to the extrusion directions, respectively. The specimen faying surfaces were dry-machined immediately prior to welding.

2.2. Inertia–friction welding

Inertia–friction welds were produced using an MTI Model 120 inertia–friction welding system. Welding parameters previously established for similar alloy welds in Al–9Fe–3Mo–1V alloy [9] were used in preliminary trials. Specific welding parameters including the moment of inertia, rotational speed and axial force were optimized through visual examination of the extruded flash and measurement of the axial displacement. Based on the results of these preliminary tests, welds for detailed characterization were produced at low, medium and high levels of axial force (Table I).

2.3. Weld characterization

Representative weld coupons were sectioned axially, mounted in epoxy and mechanically polished down to 0.3 μm alumina followed by a final polish using an 0.06 μm colloidal silica suspension. Following defect analysis of the as-polished surface using light microscopy, the metallographic specimens were etched with

TABLE I. Inertia–friction welding parameters* and results of weld-tensile and three-point guided bend tests

Inertia–friction welding			Tensile test			Bend test
Spec. Type	Axial force (kN)	Axial displacement (mm)	YS (MPa)	UTS (MPa)	El. (%)	Fracture site† (mm from IF)
LAF-1	97.8	2.78	278.0	335.8	3.7	0.25
LAF-2	97.8	2.78				
MAF-1	126.6	6.35	266.7	323.5	4.2	0.2
MAF-2	126.6	5.56				
HAF-1	153.6	11.91	294.5	345.5	2.4	0.2
HAF-2	153.6	9.92				

* Moment of inertia = 0.16588 kg m^2; angular speed = 366.5 rad s^{-1}; inertial energy = 11.134 kJ.

† All bend- and tensile-test failures occurred in Al–9Fe–3Mo–1V. The numbers in the column denote distance from the fracture initiation site to the weld interface for guided bend-test specimens.

Keller's reagent and examined using both light microscopy and SEM.

The weld interface region of welds produced with low and high axial force were examined in detail using a JEOL-200CX TEM operated at 200 kV and equipped with a Tracor-Northern TN-2000 energy-dispersive X-ray spectrometer (EDS). Thin foils for TEM analysis were produced from 0.3-mm-thick slices carefully sectioned along the weld longitudinal axis using a diamond saw and thinned to a thickness of 0.1 mm by grinding with 600 grit SiC paper. Discs 3 mm in diameter were subsequently punched from the unaffected base metal and weld interface regions at the centre and outer periphery of each weld, and twin-jet electropolished in a solution of 1 part nitric acid in 3 parts methanol at $-30\,^{\circ}C$. The thin foils were removed just prior to perforation and ion-beam milled to increase the size of the electron-transparent region. TEM examination involved imaging under bright-field and dark-field conditions and EDS analysis at selected locations.

Quantitative compositional analysis across the weld interface was also obtained using a Camica S X-50 electron probe micro-analysis (EPMA) system. Compositional analysis was performed utilizing a 1-μm-diameter probe size in order to minimize the effect of reaction volume on the quantitative data.

Knoop micro-hardness (KHN) traverses were performed across the weld interface at both the weld axial centre and outer periphery using a 200 g load, with the longitudinal axis of the indenter oriented parallel to the weld interface. Tensile tests were performed on cylindrical, transverse-weld-oriented specimens (6.35 mm gauge diameter, 25.4 mm gauge length) machined from the half radius of the welded coupons and tested as per ASTM E-8-89a at an extension rate of 4.2×10^{-3} mm s^{-1}. Additionally, three-point guided bend testing was performed to identify preferential failure locations. Testing was performed on longitudinal sections (weld flash removed) with the flat surface (weld centre) placed in tension. Finally, SEM fractographic analysis was performed on the three-point bend-test specimens.

3. Results

3.1. Microstructure of Al–9Fe–3Mo–1V and IM 2024–T351 base materials

Light microscopy analysis of the Al–9Fe–3Mo–1V base metal showed both dark- and light-etching regions (Fig. 2a). Examination at higher magnification

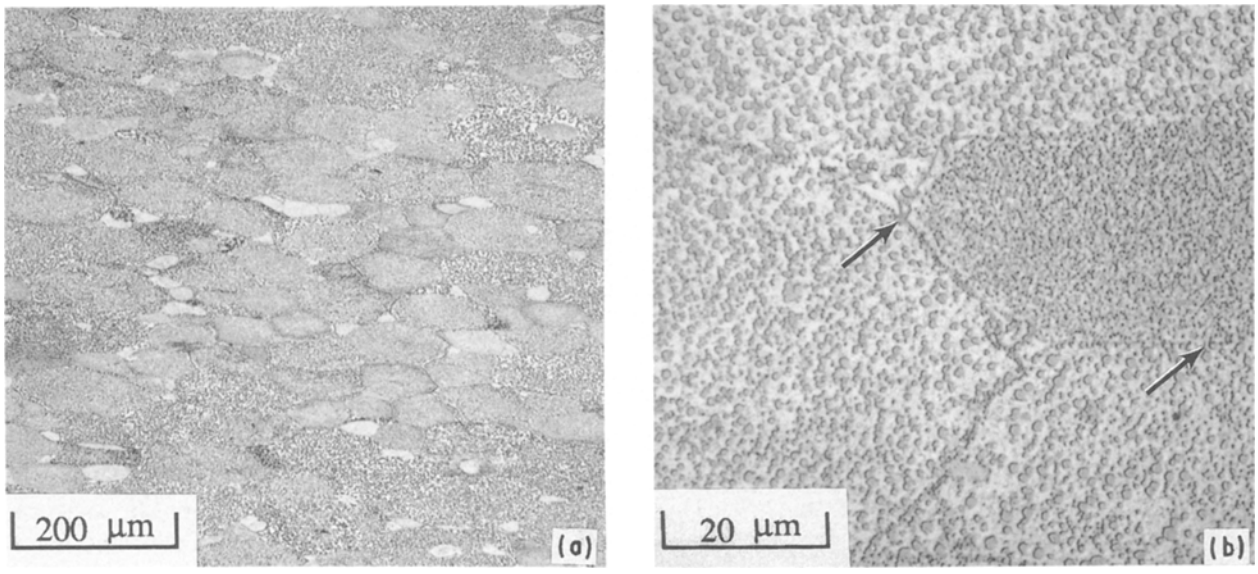

Figure 2 Light micrographs of Al–9Fe–3Mo–1V base metal. Arrows in (b) indicate boundary between powder particles.

(Fig. 2b) revealed that the observed differences in contrast resulted from variations in the size and distribution of the dispersoid particles. Boundaries between the individual powder particles (arrows in Fig. 2b) were clearly delineated, suggesting limited particulate deformation during extrusion.

TEM examination revealed three different base metal dispersoid morphologies (Fig. 3a, b), i.e. coarse, spherical dispersoids ranging from 500–1000 nm in diameter; fine, acicular dispersoids ranging from 200–1000 nm in length; and small, spherical dispersoids ranging from 100–250 nm in diameter. Previous electron microscopy and X-ray diffraction analysis of this Al–Fe–Mo–V alloy [10] indicated that the coarse spherical dispersoids are enriched in Al, Mo and V, and are likely to be $Al_{12}Fe_3$(Mo, V). The small spherical dispersoids, which were enriched in both Mo and V, were probably Al_6Fe type, while the acicular particles were Al_3Fe type. EDS analysis performed on the dispersoids in this study corroborated the results in this previous work. TEM examination at higher magnification of selected regions containing fine dispersoid particles (regions of dark contrast in Fig. 2a) showed a near absence of acicular particles (Fig. 3c, d). These regions probably originated from fine powder particles which underwent rapid solidification to extremely fine dendritic alpha aluminium.

Light microscopy of the IM 2024–T351 alloy showed elongated alpha aluminium grains decorated by dark-etching grain boundary dispersoids (Fig. 4a). In addition, several fine, dark-etching particles were observed within the alpha aluminium grains. Examination of the grain-boundary particles at higher magnification (Fig. 4b) revealed agglomerations of different types of dispersoids. Consistent with the T351 temper, TEM bright-field imaging (Fig. 4c, d) showed sub-grains within the elongated alpha aluminium grains and two types of intergranular particles. Based on the morphology of these particles and EDS analysis, the small lath-type precipitates and the large, columnar-shaped particles were identified as precursor S′ particles (Al_2CuMg) and $Al_{20}Cu_2Mn_3$, respectively. Despite extreme care, the coarse, agglomerated dispersoids observed at the alpha aluminium grain boundaries (Fig. 4b) underwent preferential attack during electropolishing and consequently were not characterized using TEM/EDS in the present study.

3.2. Weld macroscopic examination

Visual examination of the welds showed an increase in the axial force to promote an increase in the axial displacement of the two workpieces (Table I), and correspondingly an increase in the volume of flash

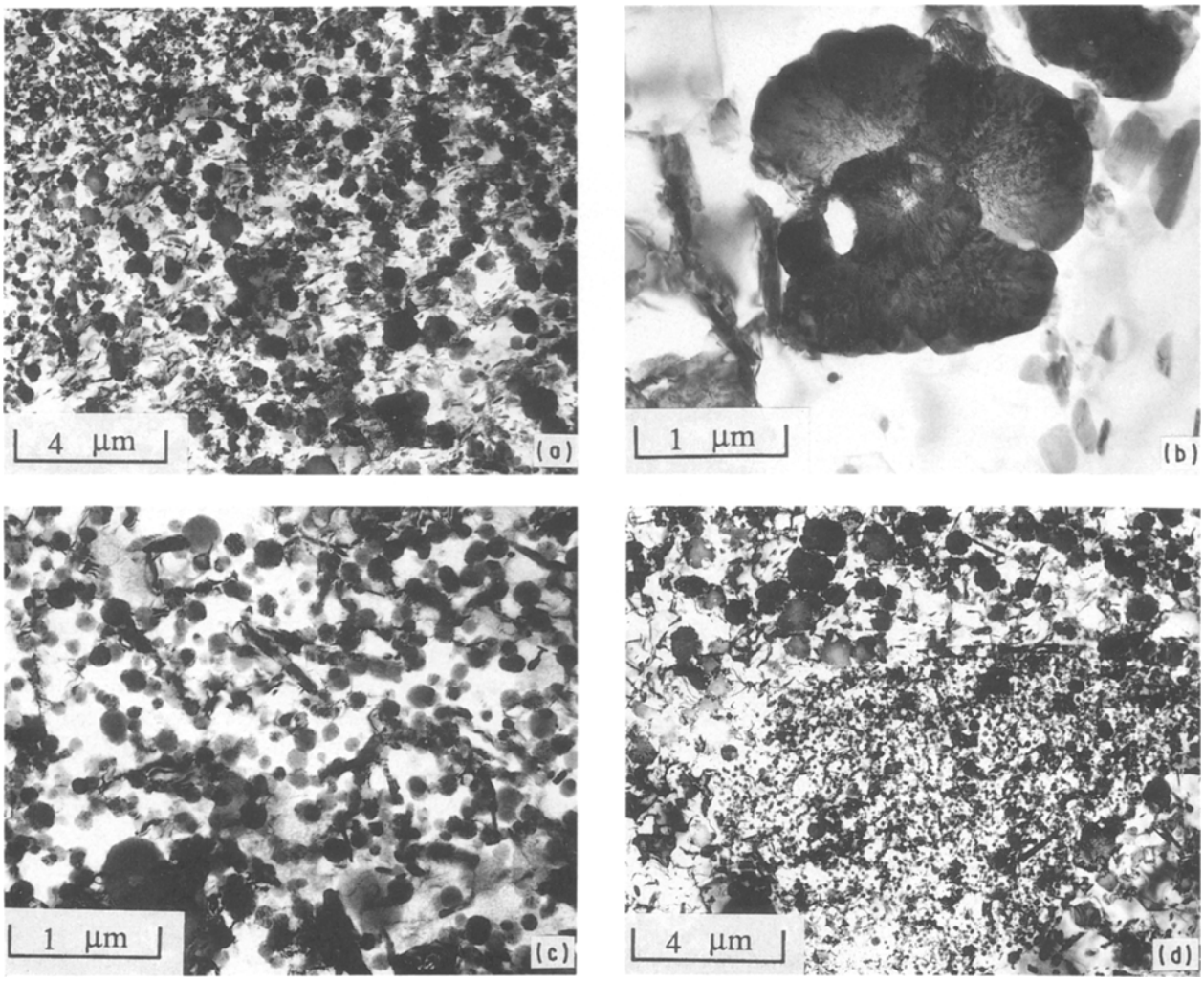

Figure 3 TEM bright-field micrographs of Al–9Fe–3Mo–1V base metal. (a, b) Predominant microstructure; (c, d) regions containing fine dispersoids.

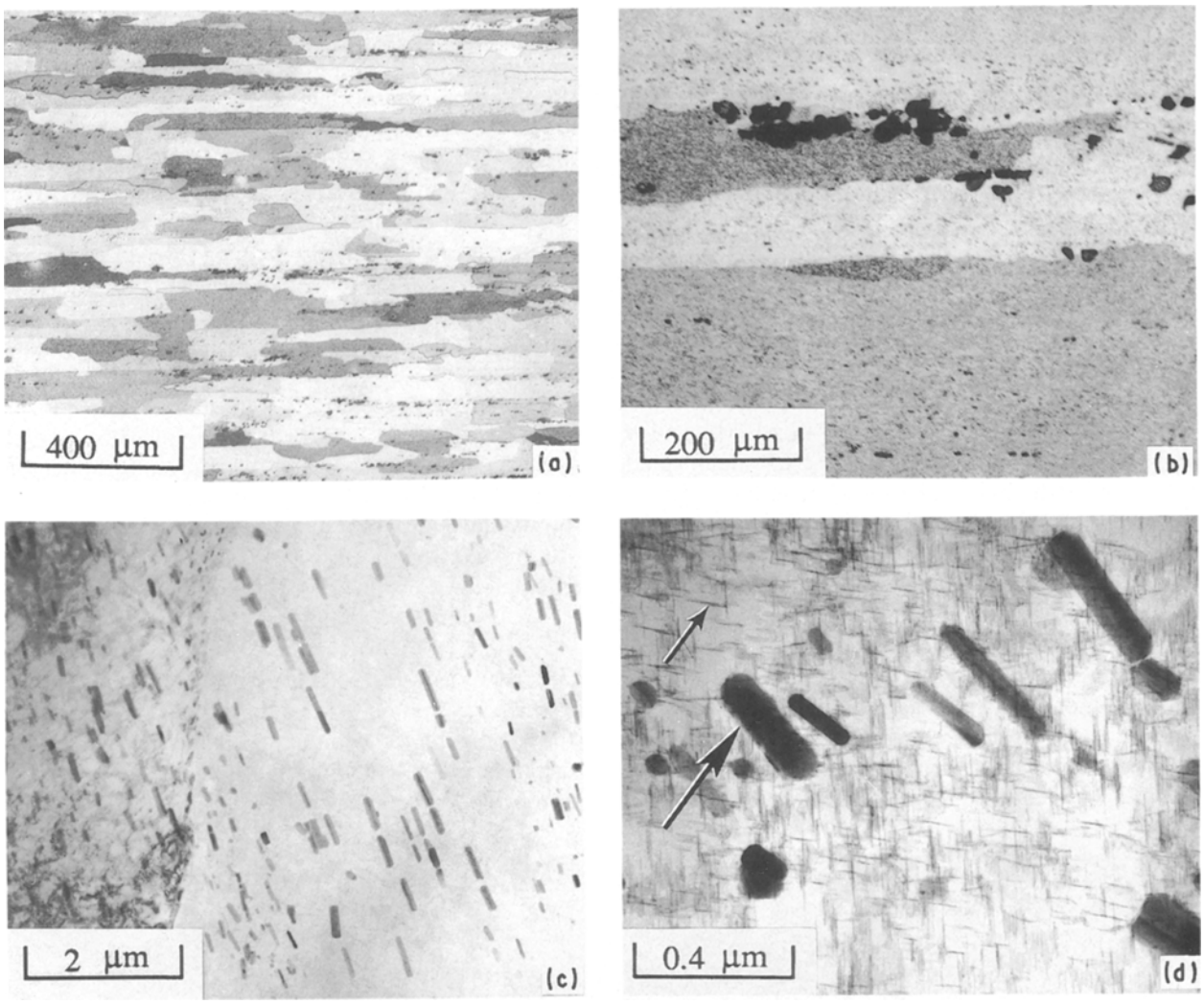

Figure 4 Light (a, b) and TEM bright-field (c, d) micrographs of IM 2024–T351 base metal. (a) Elongated alpha grain structure; (b) higher magnification showing grain boundary particles; (c) sub-grain boundary and columnar $Al_{20}Cu_2Mn_3$ particles; (d) fine S′ precipitates (small arrow) and large columnar $Al_{20}Cu_2Mn_3$ particles (large arrow).

extruded from the weld interface. This analysis also revealed the extrusion of flash to be minimal from the Al–9Fe–3Mo–1V but appreciable from the IM 2024–T351, an observation consistent with the relatively lower elevated-temperature strength of the precipitation-hardened IM alloy. Macroscopic examination of the weld axial cross sections showed that increased weld axial force promoted a progressive transition in the shape of the weld interface (Fig. 5a–c). While the low axial force weld exhibited a nearly flat interface (Fig. 5a), the medium and high axial force welds exhibited increasingly curved interfaces concave into the Al–9Fe–3Mo–1V (Fig. 5b, c). Heavy etching of the welds revealed the presence of HDZs on both sides of the weld interface, with the extent and width of this region greatest in the IM 2024–T351. The HDZ on either side of the weld interface exhibited a parallel shape at low axial force which took on an increasingly hour-glass shape at higher axial force, particularly in the IM 2024–T351. As shown in Fig. 5c, the HDZ width was minimal at the axial centre line of the weld produced at the highest axial force.

3.3. Weld microstructure characterization

3.3.1. Light microscopy analysis

Light microscopy examination at increased magnification more clearly delineated microstructure transitions in each alloy from the unaffected base metal to the weld interface (Figs 6 and 7). In Al–9Fe–3Mo–1V, which did not exhibit a strong base-metal texture, the microstructure gradually became flattened in a direction parallel to the weld interface. In the welds produced using low axial force (Fig. 6a, b), the width of this deformed region was greatest at the weld centre as opposed to the outer periphery. Near the weld interface, local deformation was sufficiently extensive that the heterogeneous base-metal microstructure appeared nearly homogeneous, particularly at the centre of the weld produced using a low axial force. The application of a higher axial force promoted an increase in the width of the structurally flattened region, but the presence of a narrow homogenized region, particularly, at the axial centre line.

Microstructural variations in the IM 2024–T351 HDZs were much more apparent. Remote from the

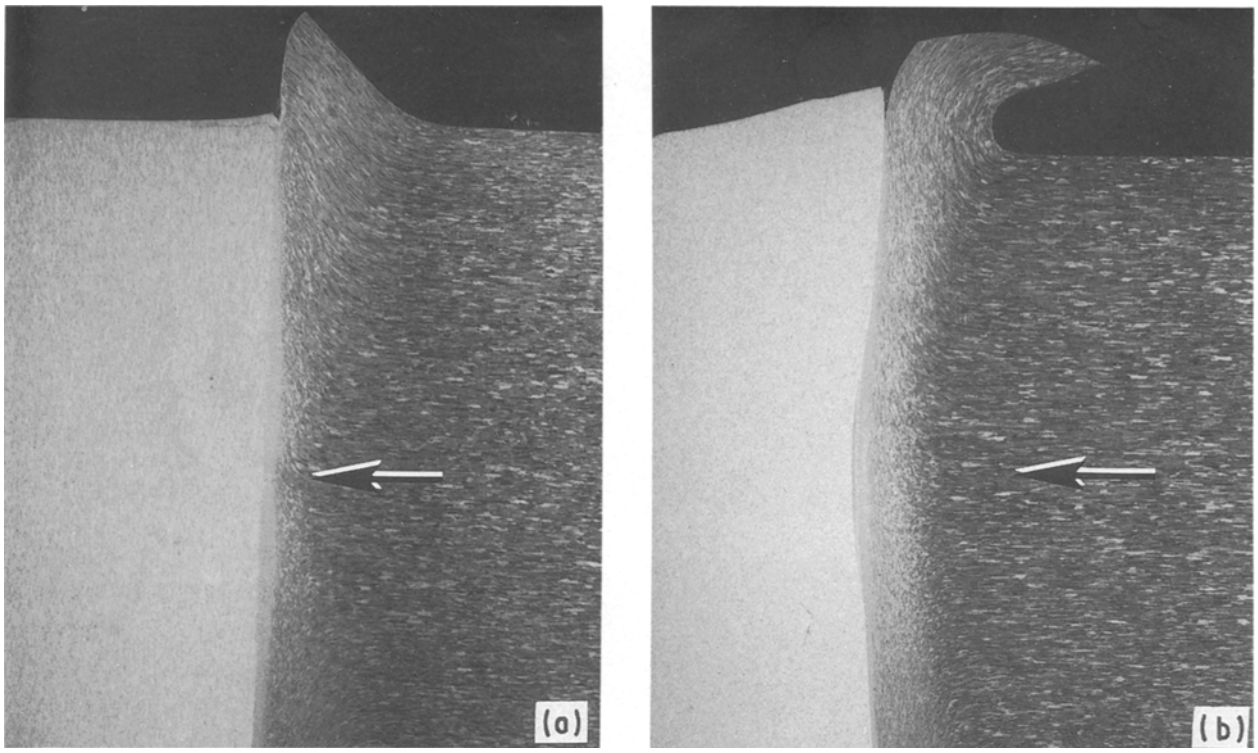

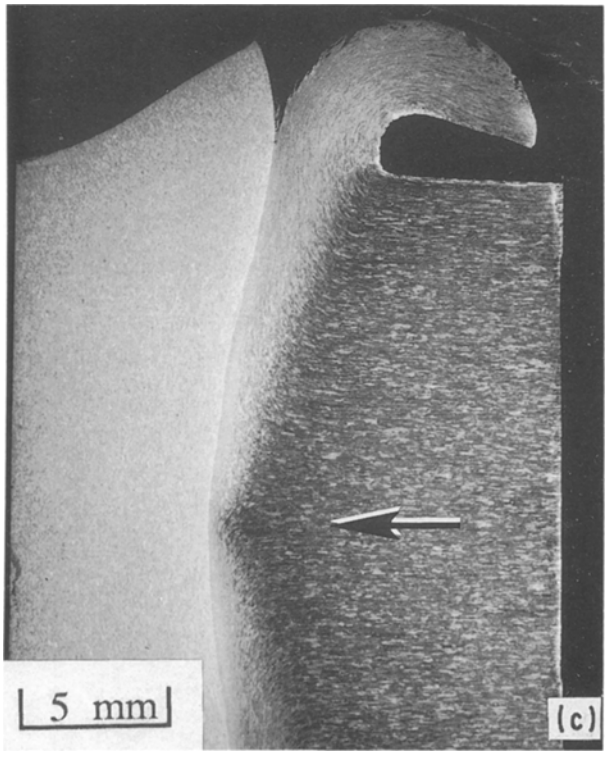

Figure 5 Light macrographs of inertia–friction welds between Al–9Fe–3Mo–1V (left side) and IM 2024–T351 (right side) produced at different axial force levels. (a) Low axial force; (b) medium axial force; (c) high axial force. Arrows indicate the axial centre line.

weld interface, the base-metal alpha grains gradually changed orientation and became parallel to the weld interface, with the region over which this transition occurred (i.e. the width of the HDZ) being greater at the outer periphery as against the axial centre line. Nearer to the weld interface, extensive deformation promoted microstructural homogenization of the grain structure, as in Al–9Fe–3Mo–1V. The widths of these homogenized HDZ regions appeared similar for all welds and weld locations. As shown in Fig. 7b, the outer periphery of the high-axial force weld also showed the presence of occasional cracks or voids oriented parallel to the interface.

Light microscopy at higher magnification of both the high and low axial force welds (Fig. 8) revealed that although appearing homogeneous at lower magnification, the HDZ directly adjacent to the weld interface still retained structural variations residual from the original base metal (and RS powder) microstructures. Fig. 8 also shows varying degrees of mechanical mixing at the interface between the dissimilar aluminium alloys. The central region of the weld produced at low axial force (Fig. 8a) showed the most significant extent of this mixing, with fine, narrow fingers of IM 2024–T351 extending into the Al–9Fe–3Mo–1V. The extent of this mixing, as delineated by light microscopy, was much less near the outer periphery of the weld produced using low axial force, and was also less across the entire interface of the weld produced using high axial force. Fig. 8 also shows stringers of intermetallic particles oriented along the deformation direction in the IM 2024–T351. These intermetallics probably originated as clusters of grain-boundary dispersoids present along grain boundaries in the base metal (Fig. 4b) which were deformed and aligned during the severe plastic deformation of this weld region.

As indicated above, dark-etching discontinuities were occasionally observed in the IM 2024–T351 near the outer periphery of the weld produced using a high axial force (Fig. 7b). The occurrence of similar linear discontinuities in IM 2024–T351 was previously reported in dissimilar inertia–friction welds with

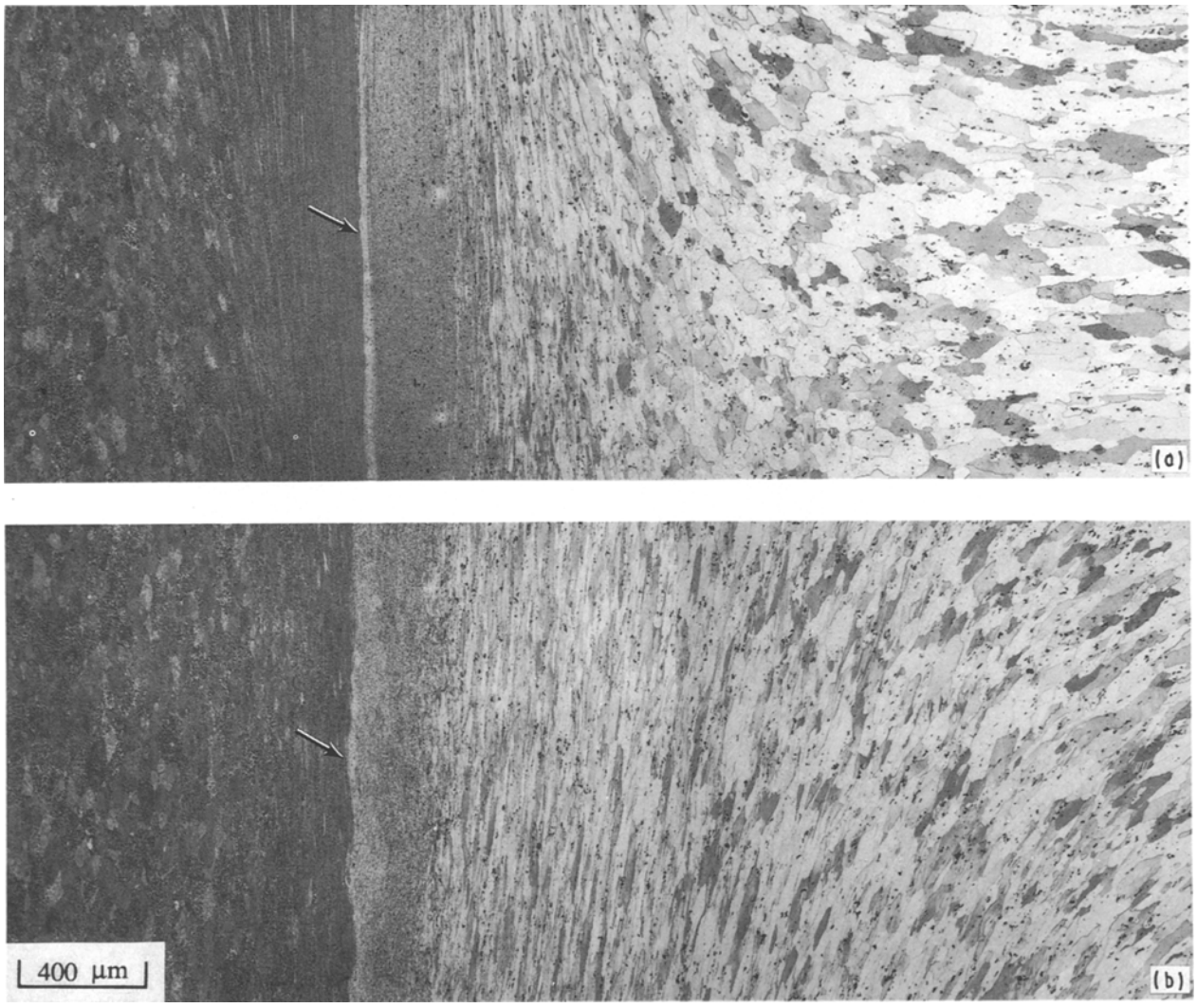

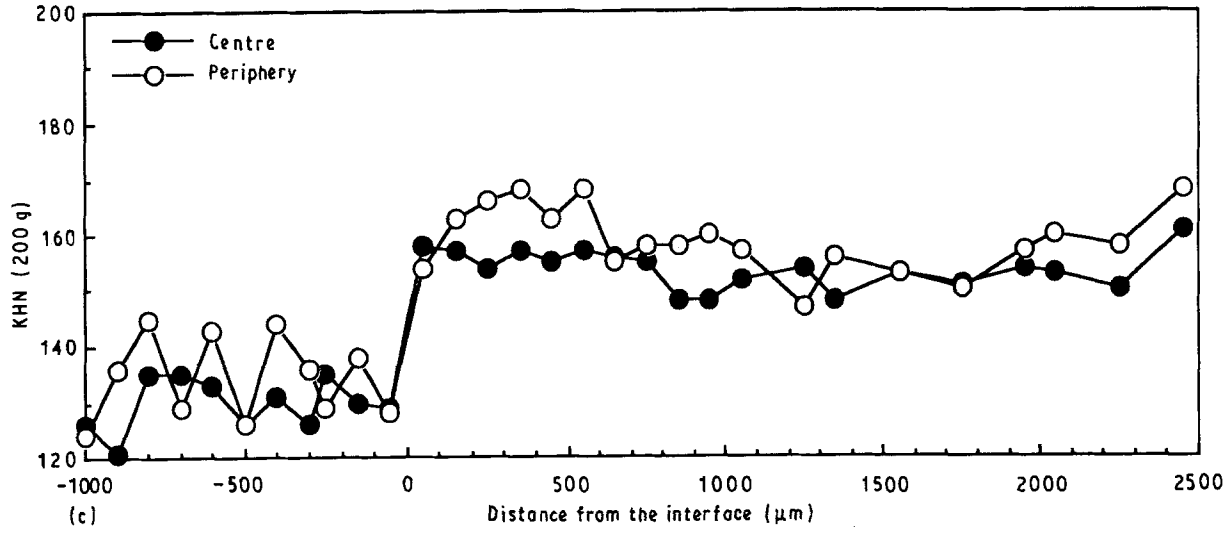

Figure 6 Light micrographs of (a) centre and (b) outer periphery regions of an inertia–friction weld produced between Al–9Fe–3Mo–1V (left side) and IM 2024–T351 (right side) at low axial force; (c) corresponding KHN hardness traverse. Arrows in (a) and (b) indicate weld interface.

Al–8Fe–4Ce [8]. Light microscopy examination of the as-polished surface of axial cross sections through the welds revealed that the linear discontinuities observed in IM 2024–T351 were pre-existing microcracks (Fig. 9a). Examination after etching with Keller's reagent showed the microcracks to be associated with grain-boundary dispersoid (intermetallic) particles (Fig. 9b). They apparently originated from the limited ductility of the intermetallic particles in combination with the severe plastic deformation observed at these

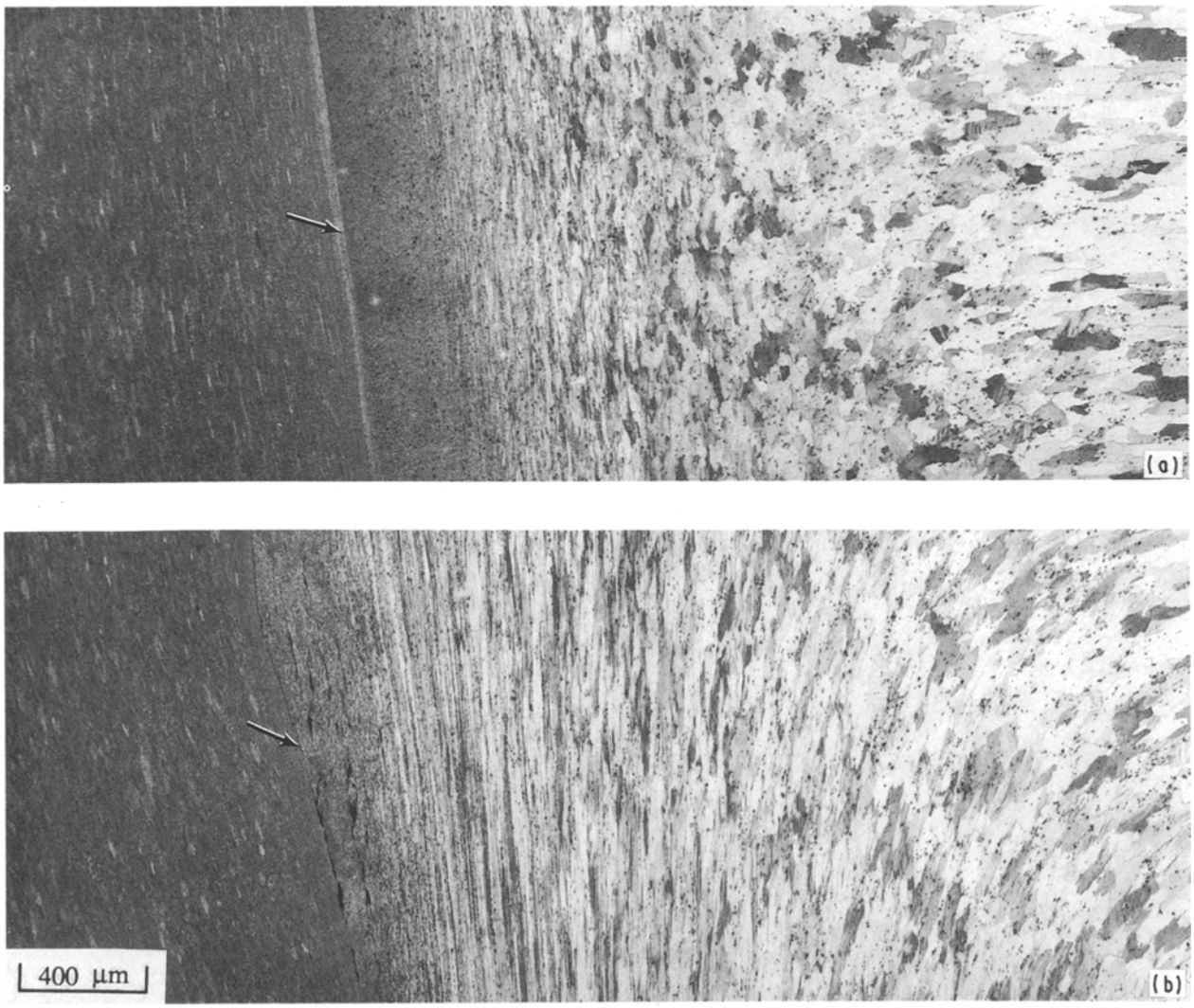

Figure 7 Light micrographs of the (a) centre and (b) outer periphery regions of an inertia–friction weld produced between Al–9Fe–3Mo–1V (left side) and IM 2024–T351 (right side) at high axial force; (c) corresponding KHN hardness traverse. Arrows in (a) and (b) indicate weld interface.

locations. An alternative mechanism for their origin may be highly localized eutectic melting along grain boundaries, although this could not be confirmed.

3.3.2. TEM analysis

Fig. 10 shows a TEM bright-field traverse across the weld interface at the centre of the low axial force weld. Traversing from the Al–9Fe–3Mo–1V side toward the weld interface (left to right in the top traverse in Fig. 10), adjacent regions showed dark and light contrast depending on the local dispersoid size and density. Regions containing a higher density of coarse dispersoids typically exhibited a darker contrast, while

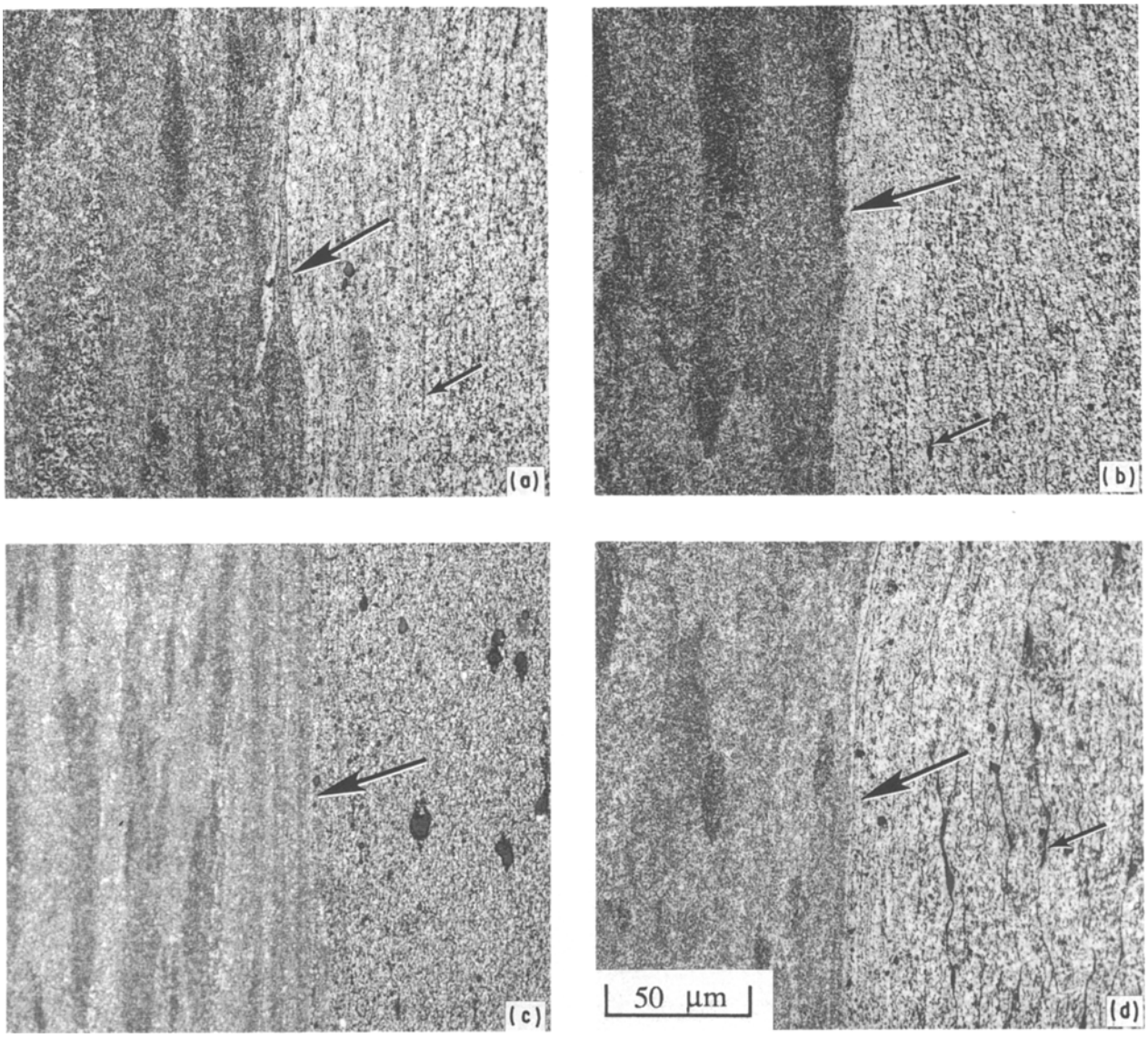

Figure 8 Light micrographs of the interface regions of inertia–friction welds produced between Al–9Fe–3Mo–1V (left side) and IM 2024–T351 (right side). (a) Centre of low axial force weld; (b) outer periphery of low axial force weld; (c) centre of high axial force weld. (d) outer periphery of high axial force weld. Small arrows indicate intermetallic stringers aligned along the deformation direction in IM 2024. Large arrow indicates weld interface.

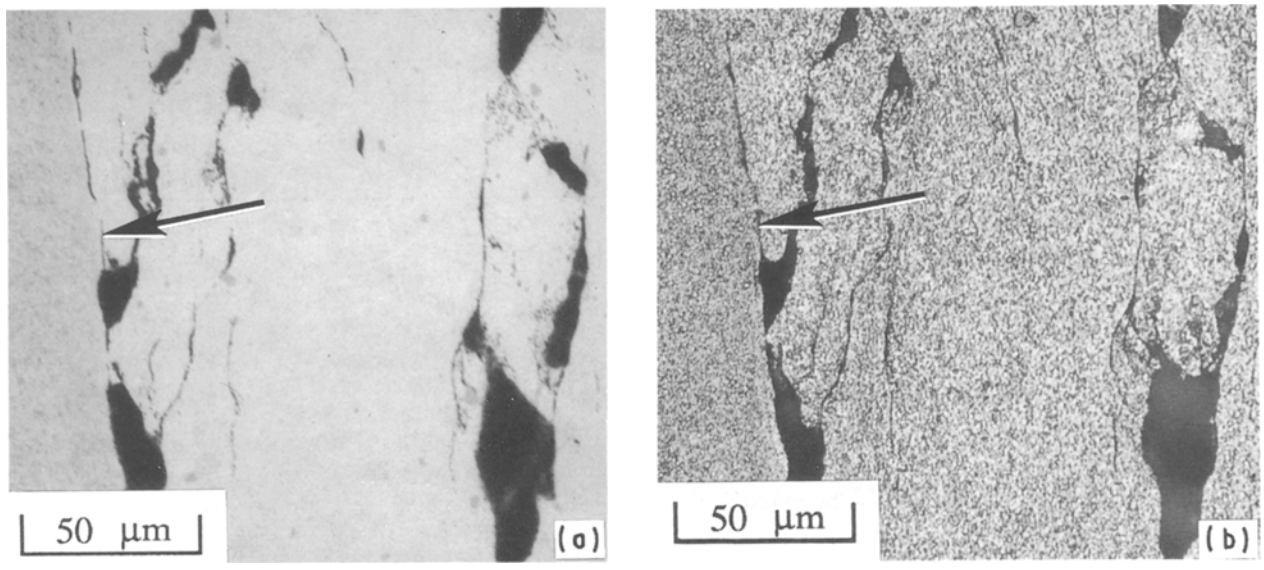

Figure 9 Light micrographs of weld defects in IM 2024–T351 at outer periphery of high axial force weld. (a) Unetched; (b) after etching with Keller's reagent. Large arrows indicate weld interface.

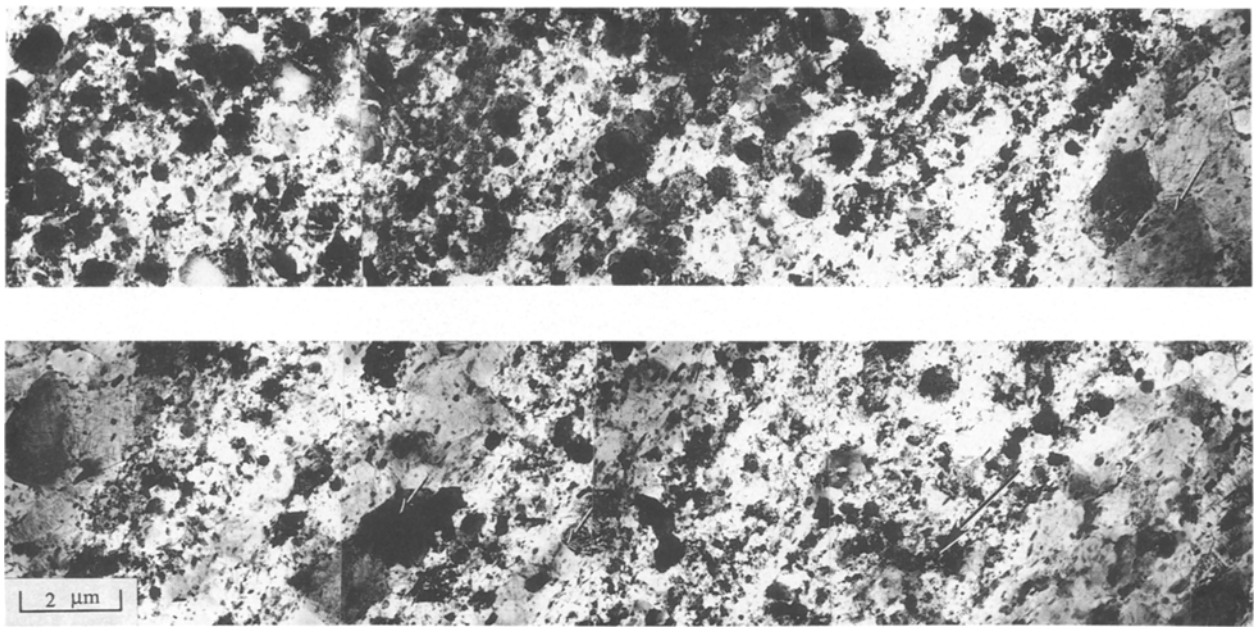

Figure 10 TEM bright-field traverse across weld interface region at centre of low axial force weld. Lower traverse is continuation of right side of top traverse. Left side of top traverse is Al–9Fe–3Mo–1V and right side of bottom traverse is IM 2024–T351. Large arrow indicates location of interface between mechanically-mixed region and IM 2024–T351. Small arrows indicate regions of IM 2024–T351 in mechanically mixed region.

regions containing finer dispersoids exhibited a lighter contrast. Examination of the region nearest to the weld interface showed an increase in the number of fine dispersoids and an absence of the coarse, spherical dispersoids. This observation was consistent with previous work [9] on the similar alloy inertia–friction welding of Al–9Fe–3Mo–1V which showed an absence of the coarse dispersoids near the weld interface due to their fracture and dispersion. Bright- and dark-field imaging of Al–9Fe–3Mo–1V directly adjacent to the weld interface showed an extremely fine-grained recrystallized alpha aluminium matrix. In the vicinity of the weld interface, alternating bands of Al–9Fe–3Mo–1V and IM 2024–T351 (small arrows) were observed, indicating highly localized mechanical mixing between the two base alloys. The Al–9Fe–3Mo–1V bands in this region were devoid of the coarse, spherical dispersoids, again indicating their fracture and dispersion. This structure gradually changed (extreme right of bottom traverse in Fig. 10) to an entirely IM 2024–T351 microstructure which exhibited fine, equiaxed alpha aluminium grains, indicating the occurrence of dynamic recrystallization during the welding cycle. In this region, the columnar $Al_{20}Cu_2Mn_3$ particles which were uniformly aligned in the unaffected base metal grains (Fig. 4c) became more randomly oriented, and the fine S′ was not in evidence due to its dissolution during the weld thermal excursion. Outside the recrystallized zone (RXZ) in the IM 2024–T351, a gradual microstructural transition from the fine grain structure to an irregular, coarse grain structure (similar to that of the base metal shown in Fig. 4d) was observed.

In comparison with Fig. 10, the TEM bright-field traverse across the interface of the low axial force weld at the outer periphery (Fig. 11) showed two significant differences. Although a random distribution of fine and coarse dispersoids was evident near the weld interface in the Al–9Fe–3Mo–1V (large arrow in Fig. 11), the number of coarse dispersoids was greater and correspondingly the density of fine dispersoids was less as compared to the weld centre, indicating a lesser extent of dispersoid breakup. A difference in the extent and nature of interface deformation at the outer periphery as opposed to the weld centre was further indicated by the minimal evidence of mechanical

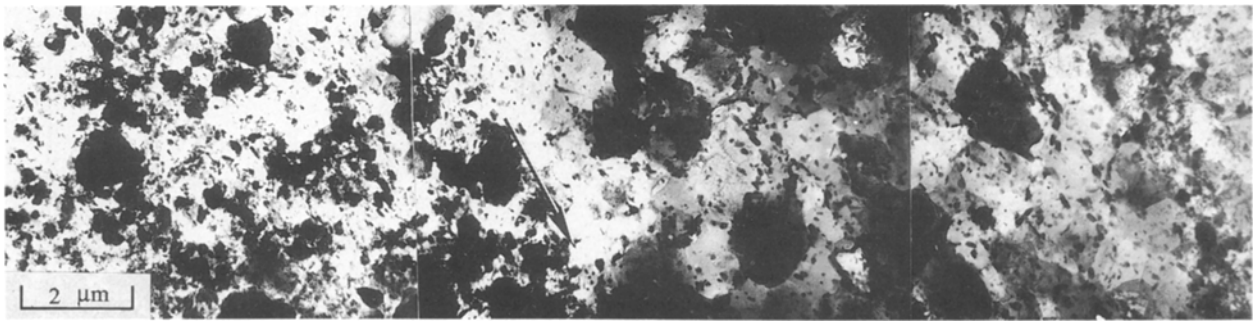

Figure 11 TEM bright-field traverse across interface near the outer periphery of the low axial force weld. Large arrow indicates location of weld interface between Al–9Fe–3Mo–1V (left) and IM 2024–T351 (right).

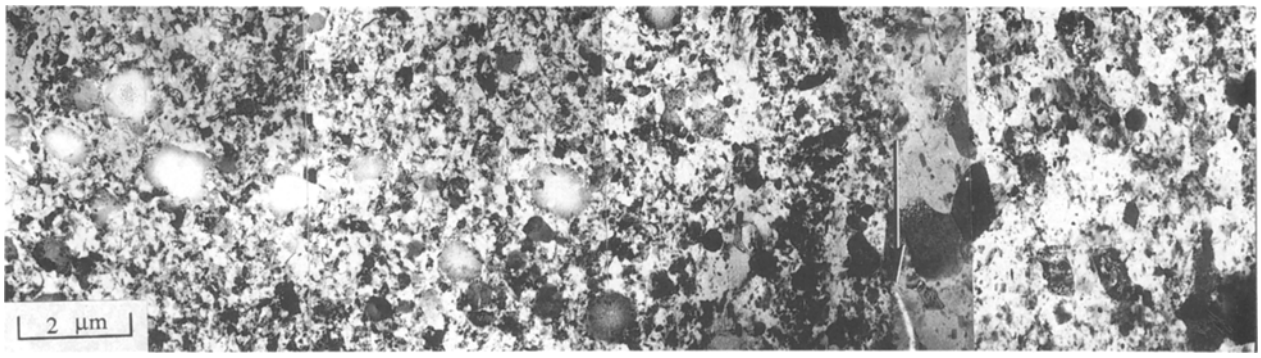

Figure 12 TEM bright-field traverse across interface at the weld centre of the high axial force weld. Large arrow indicates location of weld interface between Al–9Fe–3Mo–1V (left) and IM 2024–T351 (right).

mixing between the IM 2024–T351 and the Al–9Fe–3Mo–1V, and the presence of a clearly defined weld interface (large arrow in Fig. 11).

Fig. 12 shows a TEM bright-field traverse across the weld interface at the centre of the high axial force weld. The Al–9Fe–3Mo–1V side of this interface showed a mixture of coarse and fine dispersoids, with an absence and possible break up of the coarse dispersoids only directly adjacent to the interface (within 5 μm of the interface). The absence of a wider dispersoid-refined region adjacent to the weld interface, as observed in the weld produced using low axial force, was consistent with light micrographs showing a very narrow HDZ at the centre of the high axial force weld. TEM examination with minimum beam tilt also revealed extremely fine, recrystallized alpha aluminium grains in both the Al–9Fe–3Mo–1V and the IM 2024–T351 (extreme right of Fig. 12) adjacent to the weld interface. Despite experiencing higher axial force, mechanical mixing between the IM 2024–T351 and Al–9Fe–3Mo–1V was minimal as compared to that observed at the centre of the low axial force weld.

TEM examination of the weld interface region at the outer periphery of the high axial force weld was

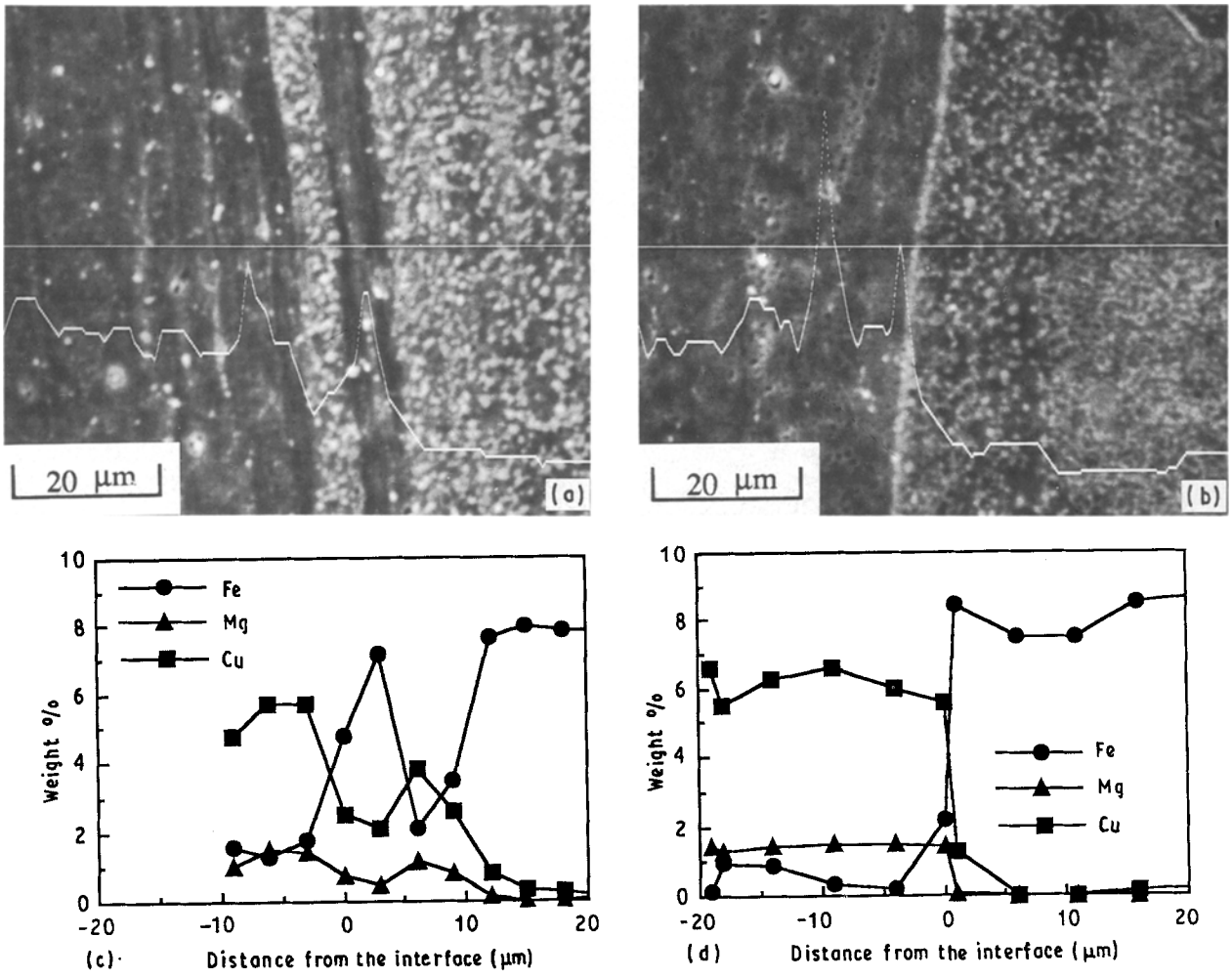

Figure 13 EPMA traverses across low axial force weld produced between Al–9Fe–3Mo–1V (right) and IM 2024–T351 (left). Straight lines in (a) and (b) are CuK_α trace scans while (c) and (d) are results of point analysis.

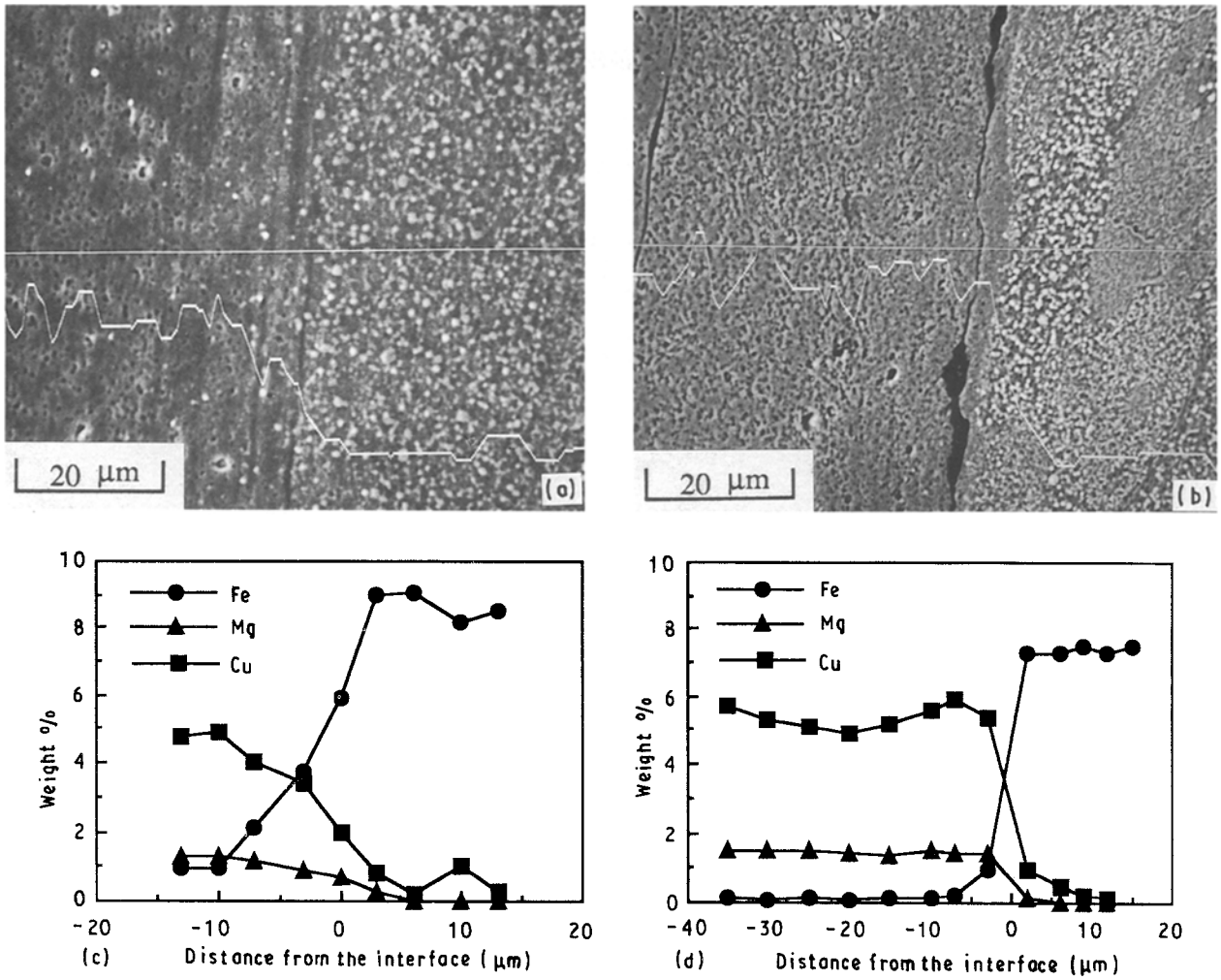

Figure 14 EPMA traverses across high axial force weld produced between Al–9Fe–3Mo–1V (right) and IM 2024–T351 (left). Straight lines in (a) and (b) are CuK_α trace scans, while (c) and (d) are results of point analysis.

not possible due to the presence of interface discontinuities which precluded the preparation of high quality thin foils.

3.3.3. EPMA analysis across weld interfaces

Figs 13 and 14 show composition profiles obtained by EPMA across the weld interface near the weld centre and outer periphery for low and high axial force welds, respectively. At the centre of the weld produced using low axial force (Fig. 13a, c), localized mechanical mixing of the two alloys promoted variations in composition across the weld interface. A more definitive interface at the outer periphery of this weld showed a correspondingly more abrupt compositional change in Fig. 13b and d. Note that the size of the volume actually sampled during the analysis, and averaging effects of the alpha matrix and the intermetallic phases, made the investigation of compositional gradients in the alpha phase due to interdiffusion (e.g. Cu into the Al–9Fe–3Mo–1V) difficult. Considering the extremely rapid thermal cycle experienced during welding, it is unlikely that such interdiffusion in the alpha matrix was significant.

At the centre of the weld produced using a high axial force, mechanical mixing between the base alloys was evidenced both in the SEM micrograph of the weld interface by a gradual change in the dispersoid density (Fig. 14a), and by the compositional variations across the interface (Fig. 14c). This mixing occurred in a uniform and more gradual manner than observed at the centre of the weld produced using low axial force. As in the weld produced at low axial force, the transition in the outer periphery was much more abrupt due to negligible mechanical mixing (Fig. 14b and d).

3.4. Weld mechanical properties

Hardness evaluation of the base metals showed an average hardness of KHN 160 (200 g load) for IM 2024–T351 and KHN 131 for Al–9Fe–3Mo–1V. Consistent with the microstructural analysis and differences in dispersoid sizes and density, the coarse-dispersoid regions in the Al–9Fe–3Mo–1V (Fig. 2b) exhibited a relatively lower hardness compared to the fine-dispersoid regions.

Figs 6c and 7c show microhardness traverses across the centre and outer periphery of welds produced using both low and high axial force, respectively. In all traverses performed, the hardness in the IM 2024–T351 and across the weld zone exceeded the lowest hardness levels recorded in the unaffected Al–9Fe–3Mo–1V (about 125 KHN), suggesting weld joint efficiencies of 100 %. In the weld produced with

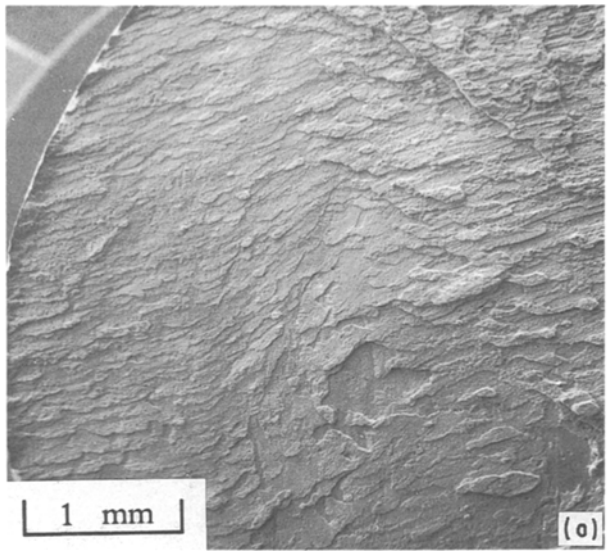

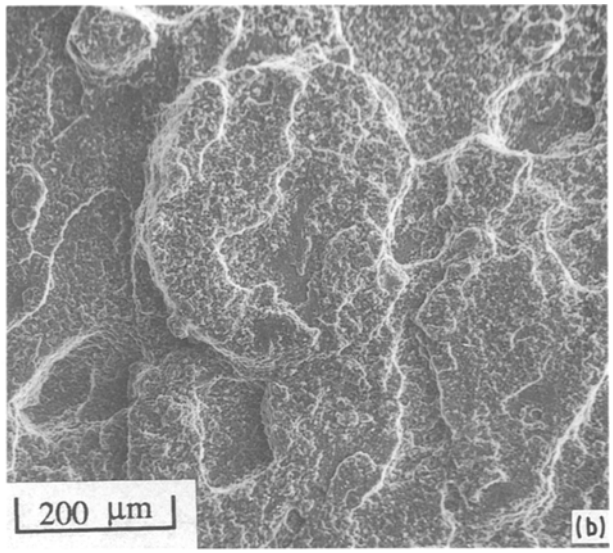

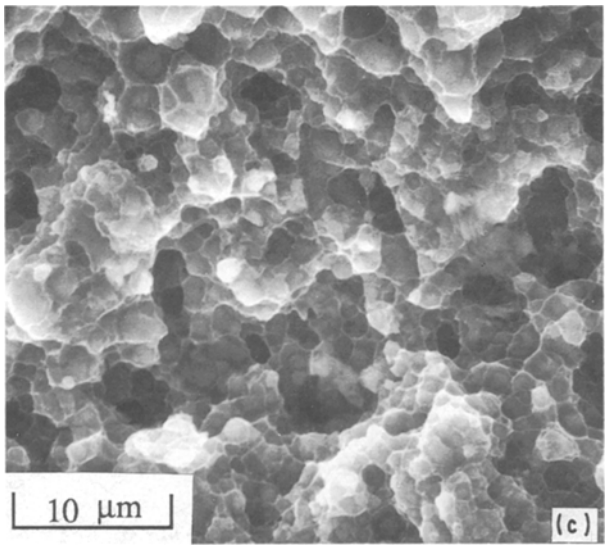

Figure 15 SEM fractographs of high axial force weld bend test specimen. (a) General view at low magnification; (b) and (c) fracture surface near specimen centre at increased magnification.

low axial force, variations in hardness of the IM and RS/PM base metals due to microstructural variations decreased nearer to the weld interface due to microstructural homogenization. It is of interest to note that in the weld produced at low axial force the hardness across the IM 2024–T351 HDZ was generally greater at the outer periphery than at the axial centre, while the reverse was observed for the weld produced using a high axial force. Considering similarities in the IM 2024–T351 HDZ microstructures for these welds, the reason for this difference was not clear.

Room-temperature tensile testing of transverse-weld oriented tensile specimens determined that failures occurred preferentially in the Al–9Fe–3Mo–1V (Table I). Although the tensile test specimens showed marginal ductility (2–4% elongation), the tensile strength of the three types of welds varied from between 323–346 MPa, indicating joint efficiencies ranging from about 85 to over 90% relative to the lower room-temperature strength Al–9Fe–3Mo–1V base alloy (tensile strength of approximately 380 MPa).

Three-point guided bend testing of axial sections through the welds was performed to determine the fracture path through the entire weld (assuming axisymmetry) since the tensile specimens only characterized fracture at a location approximately midway between the axial centre line and the outer periphery. Analysis of failed bend specimens revealed preferential fracture initiation and propagation through the Al–9Fe–3Mo–1V HDZ, with negligible evidence of macroscopic plastic deformation. It is of interest to note that despite the presence of micro-cracks in the IM 2024–T351 at the outer periphery of the high axial force weld, failure initiated in softer Al–9Fe–3Mo–1V.

3.5. Fracture characteristics

As indicated above, metallographic analysis indicated fracture of the dissimilar welds to occur through the lower strength Al–9Fe–3Mo–1V alloy. Fractographic characteristics of bend specimens produced from welds generated using low and high axial forces generally appeared quite comparable. Fig. 15 shows the characteristics of a typical fracture surface for a bend-test specimen produced from a high axial force weld. At low magnification, the fracture surface exhibited a relatively flat topography and a unidirectional texture across the fracture face. This texture may be related to the extrusion direction of the base metal, which was perpendicular to the longitudinal specimen length and therefore parallel to the weld interface. This observation suggests a fracture path outside the central HDZ region. If fracture had occurred near the centre of the HDZ, a macroscopic fracture surface exhibiting an outward spiral typical of inertia–friction welds should have been observed. The analysis of this surface at increased magnification clearly showed fracture initiation by microvoid formation at dispersoid/alpha aluminium interfaces and final ductile rupture of alpha aluminium matrix (Fig. 15b, c).

4. Discussion

The inertia–friction welding process is very amenable to the joining of similar and dissimilar alloys which

cannot be welded using fusion processes. During dissimilar alloy inertia–friction welding, one alloy generally maintains a higher yield strength throughout the entire range of temperatures experienced at or near the weld interface. In contrast, the present study involved a unique case in which a strength reversal occurred as the temperature increased from room temperature, where the IM 2024–T351 alloy was the strongest, to elevated temperatures where the RS/PM Al–9Fe–3Mo–1V alloy was the strongest (Fig. 1).

The cylindrical specimens joined using the inertia–friction welding process experienced complex combinations of axial and torsional forces and stresses across the weld interface. In conventional inertia–friction welds between the same material, the plastic flow of metal heated by frictional heating occurs from the axial centre line of the weld out toward the outer periphery in a spiral pattern. In the present work, such metal flow and deformation was observed to be relatively uniform in the HDZ remote from the weld interface, particularly within the microstructurally flattened regions observed in both alloys. In the vicinity of the interface, however, non-uniform deformation both within the HDZ of each respective alloy and highly localized mechanical mixing directly at the interface between the dissimilar alloys was very complex. In the present work, the nature and extent of this mechanical mixing was highly dependent on both the axial force and the location within the weld.

In the dissimilar Al–9Fe–3Mo–1V/IM 2024–T351 inertia–friction welds, differences in the strength of the two alloys between room and elevated temperatures appeared to influence both the macroscopic and microscopic characteristics of the weld. In considering the origins of the observed macrostructures and microstructures, it is important to understand the influence of the welding process on the local temperature and pressure distribution across the interface. During inertia–friction welding, a larger quantity of frictional heat is generated near the outer periphery than at the centre (arising from differences in the relative velocity of the specimens at these two locations). Therefore a higher peak temperature occurs at the outer periphery as against the specimen centre. In contrast, normal compressive stresses at the outer periphery of the weld may be lower than at the axial centre line due to a 'friction hill effect', as in plane-strain forging. The combination of these velocity and pressure differences can actually promote peak temperatures at a location near but not directly at the outer periphery of the weld interface.

Macroscopically, the IM 2024–T351 penetrated into the Al–9Fe–3Mo–1V, thereby promoting a concave interface particularly at the high axial force level, despite the appreciably greater expulsion of the IM 2024–T351 as flash. Considering the aforementioned differences in heating across the weld interface, it is suggested that the relatively low peak temperatures experienced just behind the weld interface at the axial centre line of the high axial force weld promoted minimal softening of the IM 2024–T351, and that the compressive strength of this region remained above that of the adjacent Al–9Fe–3Mo–1V into which it macroscopically penetrated. The presence of a steep temperature gradient and narrow high-temperature region at this location was consistent with the hourglass shape of the high axial force weld. Toward the outer periphery of the weld, higher temperatures generated at the interface promoted the strength reversal shown in Fig. 1 and rapid softening of the IM 2024–T351. The rapid softening of the IM 2024–T351 relative to the stronger Al–9Fe–3Mo–1V resulted in appreciable deformation and in a large quantity of flash being extruded from the IM 2024–T351, as observed in Fig. 5.

Variations in temperature and pressure across the weld interface also explain the origin of microstructural characteristics along the interface. Light and TEM microscopy analysis revealed significant mechanical mixing of the two alloys at the interface near the axial centre line, particularly in the low axial force weld. Rao *et al.* [11] reported that mechanical mixing during friction welding originates from the interlocking of initial asperity peaks at the specimen faying surfaces and subsequent formation of wedges and smearing of wedges. This action occurs on an extremely fine scale, and may account for some of the mixing observed with TEM. The more macroscopic mechanical mixing observed both with light microscopy and TEM at the centre of the low axial force weld may further be related to differences in the tensile strengths of the alloys at high temperatures, and the influence of these strength differences on the non-uniform deformation experienced at this interface.

Considering the aforementioned difference in welding pressure across the interface, the decrease in mechanical mixing near the outer periphery was anticipated. However, the greater extent of mixing observed in the low as opposed to the high axial force weld was not easily explained. This difference in mixing may be attributed to differences in the uniformity of deformation at this location and/or the duration of the welding cycle.

In general, the extent of coarse dispersoid fracture and dispersion in the Al–9Fe–3Mo–1V was appreciably less than that observed previously for similar alloy welds produced at comparable axial force levels [9]. In addition, the RS/PM alloy HDZ showed no evidence of dispersoid-free regions which formed near the outer periphery of similar alloy welds due to extremely non-uniform deformation at and near the weld interface. Both of these phenomena are related to the complex stresses experienced at the weld interface and the manner in which the material responds to these stresses via deformation. It is proposed that the appreciably softer IM 2024–T351 accommodated more deformation and thereby promoted less extensive, and perhaps more uniform deformation in the higher-strength Al–9Fe–3Mo–1V, thereby precluding the occurrence of these phenomena.

Although the parametric analysis performed in this study was very limited, weld tensile property analysis indicated very high weld joint efficiencies exceeding 90% for the optimum welding conditions. No rationale for the inability to achieve 100% joint efficiencies despite an absence of hardness degradation across the

weld zone was apparent. The observation of fracture in the weld HDZ away from the weld interface indeed suggests that a highly localized softened region may have existed which was not revealed by hardness testing or microscopy. Acceptable hardness levels across the weld zone were promoted by an effective absence of visible dispersoid coarsening in the RS/PM alloy and the dynamic recrystallization of the alpha grains near the interface in both alloys. This recrystallization and the generation of an extremely fine alpha grain size were most important within the IM 2024–T351 HDZ in which the strengthening S′ precipitates had been resolutionized during the rapid weld heating and cooling cycle. Although not performed in this study, the low-temperature ageing of the weld may further strengthen the IM 2024–T351 HDZ due to the reprecipitation of this phase.

5. Conclusions

1. High-integrity weld joints were produced between RS/PM Al–9Fe–3Mo–1V and IM 2024–T351 using the solid-state inertia–friction welding process.

2. Differences in the strength of the Al–9Fe–3Mo–1V and IM 2024–T351 alloys at room as opposed to elevated temperatures promoted a curved weld interface concave into the Al–9Fe–3Mo–1V and the formation of weld flash principally from the IM 2024–T351.

3. Weld axial force significantly influenced the appearance of the weld interface, characteristics of the weld HDZ, joint integrity and the occurrence of weld defects.

4. The weld interface was characterized by highly localized mechanical mixing of the dissimilar aluminium alloys, with the extent of this mixing most significant near the axial centre line of the weld produced using low axial force. The weld interface was bounded by heat- and deformation-affected zones (HDZs) comprised of extremely fine alpha aluminium grains (1–2 μm) and fine dispersoid particles.

5. Knoop hardness testing revealed an absence of hardness degradation across the weld interface. Transverse-weld oriented tensile testing determined joint efficiencies of 85–90%, and fracture in the Al–9Fe–3Mo–1V HDZ. This location also served as the preferential fracture path for three-point guided bend test specimens.

Acknowledgements

The authors are indebted to Dr Walter Griffith of the Wright Laboratories at WPAFB, Ohio for providing the Al–9Fe–3Mo–1V alloy. Appreciation is also expressed to Messrs M. Shalosky, P. Griffin, E. Barnhouse, T. Smith, J. Davis and J. Banal for their assistance in inertia–friction welding and Mr Hendrick Colijn and Mr David Little of OSU for assistance in EDS and EPMA analysis, respectively. The investigation was performed with financial support from the Army Research Office under contract No. DAAL03-88-K-0049.

References

1. W. E. QUIST and R. E. LEWIS, in "Rapidly Solidified Powder Aluminium Alloys, STP 890", edited by E. A. Starke Jr and M. E. Fine (American Society for Testing and Materials, Philadelphia, 1986) p. 7.
2. C. M. ADAM and R. G. BOURDEAU, in "Rapid Solidification Processing: Principles and Technologies", edited by R. Mehrabian, B. H. Gear and M. Cohen (Claitors, Baton Rouge, 1980) p. 246.
3. E. P. CONE and P. M. KOMATER, in "Exploratory Development of Processing Elevated Temperature Powder Metallurgy Alloys", (AFWAL-FR-18804-7, 1988) p. 6.
4. Metals Handbook, 9th edn, Vol. 2 (American Society for Metals, Materials Park, Ohio, 1983) p. 75.
5. S. KRISHNASWAMY and W. A. BAESLACK III, in "Recent Trends in Welding Science and Technology", edited by S. A. David and J. M. Vitek (ASM International, Materials Park, Ohio, 1990) p. 631.
6. W. A. BAESLACK III and S. KRISHNASWAMY, in "Advances in Welding Science and Technology", edited by S. A. David, (ASM International, Materials Park, Ohio, 1987) p. 357.
7. W. A. BAESLACK III, K. H. HOU and J. H. DEVELETIAN, *J. Mater. Sci. Lett.* **7** (1988) 944.
8. W. A. BAESLACK III and K. S. HAGEY, *Weld. J. Res. Suppl.* **67** (1988) 139s.
9. K. H. HOU and W. A. BAESLACK III, *J. Mater. Sci.* **25** (1990) 2642.
10. S. L. LANGENBECK and R. A. RAINEN, in "Elevated Temperature Aluminium Alloy Development", (AFWAL-TR-86-4027, 1986) p. 6.
11. M. RAO and T. HAZLETT, *Weld. J. Res. Suppl.* **49** (1970) 181s.

Received 21 February
and accepted 1 July 1991